PAPER

Check for updates

Origin of the low conversion efficiency in Cu$_2$ZnSnS$_4$ kesterite solar cells: the actual role of cation disorder†

Wei Chen, [ID] [a] Diana Dahliah, [ID] [a] Gian-Marco Rignanese [ID] [a] and Geoffroy Hautier [ID] ⋆[ab]

The controversial role of cation disorder in the extraordinarily low open-circuit voltage (V_{OC}) of the Cu$_2$ZnSnS$_4$ (CZTS) kesterite absorber is examined through a statistical treatment of disorder within the cluster-expansion method. It is demonstrated that the extensive Cu–Zn disorder alone cannot be responsible for the large Urbach tails observed in many CZTS solar cells. While the band gap is reduced as a result of the Gaussian tails formed near the valence-band edge due to Cu clustering, band-gap fluctuations contribute only marginally to the V_{OC} deficit, thereby excluding Cu–Zn disorder as the primary source of the low efficiency of CZTS devices. On the other hand, the extensive disorder stabilizes the formation of Sn$_{Zn}$ antisite and its defect complexes, which as nonradiative recombination and minority carrier trapping centers dominate the V_{OC} loss in CZTS. Our analysis indicates that current CZTS devices might have already approached the maximum conversion efficiency (14%) given the limited growth conditions and the remnant cation disorder even after postannealing. In view of the improved efficiency achieved with CZTS-derived kesterite absorbers, the methodology presented in this work offers an avenue to understanding and optimizing these emerging kesterite solar devices towards higher efficiency.

Broader context

Cation disorder has been often blamed for the poor power conversion efficiency of kesterite solar cells, which remains at a very low level compared to other thin-film technologies despite years of optimization. The role of cation disorder has been questioned by recent experiments showing that a higher degree of ordering does not necessarily improve the open-circuit voltage. By unraveling the actual roles of cation disorder in the Cu$_2$ZnSnS$_4$ kesterite absorber through a statistical treatment of disorder combined with first-principles calculations, our work pinpoints the origin of the persistently low efficiency to the disorder-assisted formation of deep centers. Our approach provides a general framework to complementing experiment where the perfect control of ordering can be challenging.

Introduction

Kesterite Cu$_2$ZnSn(S,Se)$_4$ (CZTSSe) is a class of earth-abundant and nontoxic materials with a direct band gap of 1.0–1.5 eV,[1] which is ideal for photovoltaic absorbers.[1–3] The major bottleneck of CZTSSe solar cells is the low open-circuit voltage (V_{OC}) (400–700 meV), which is somehow unexpected from the nominal band-gap value.[4–6] As a result, kesterite solar cells suffer from an underwhelming power conversion efficiency topping at 12.6%,[4]

lagging well behind silicon and other thin-film technologies. The large V_{OC} deficit has been tentatively attributed to the cation disorder, which is prevalent among kesterite absorbers.[5,7,8] It has been established that the extensive Cu–Zn disorder is responsible for the redshift of the band gap at elevated temperatures,[7,9] a consequence that is rationalized by the presence of shallow antisite acceptors (Cu$_{Zn}$/Zn$_{Cu}$). Nevertheless, it is still a subject of debate as to whether cation disorder deteriorates the performance of CZTSSe solar cells. While cation disorder has been designated as the source of the unusually large band tails of CZTS,[10] there appears mounting experimental evidence showing no direct correlation between cation disorder and large band tails.[11,12] Counterintuitively, some experiments further suggest that the V_{OC} deficit is unaffected by the degree of disorder present in CZTSSe.[5,13–15]

[a] *Institute of Condensed Matter and Nanoscicence (IMCN), Université catholique de Louvain, Louvain-la-Neuve 1348, Belgium*

[b] *Thayer School of Engineering, Dartmouth College, Hanover, New Hampshire, 03755, USA. E-mail: geoffroy.hautier@dartmouth.edu*

† Electronic supplementary information (ESI) available. See DOI: 10.1039/d1ee00260k

This journal is © The Royal Society of Chemistry 2021

Energy Environ. Sci., 2021, **14**, 3567–3578 | **3567**

The difficulty in addressing the exact role of cation disorder in part stems from the practical limitation that a completely ordered CZTS cannot be achieved *via* thermal treatments (*e.g.* slow cooling).[16] The properties of fully ordered CZTS thus cannot be directly accessible from experiment. The characterization of Cu–Zn ordering is further complicated by the isoelectronic Cu^+ and Zn^{2+}, which are not distinguishable by conventional X-ray diffraction. More elaborate methods such as neutron diffraction[17] or anomalous X-ray diffraction[18] need to be used to probe directly the cation ordering.

From a theoretical standpoint, the identification of the origin of tail states and the V_{OC} deficit in CZTSSe is complicated by the fact that the extensive cation disorder requires an adequate treatment over all possible configurations with a system of considerable size. Here, by the statistical cluster-expansion (CE) technique and first-principles calculations, we unravel the role of cation disorder in the low V_{OC} of CZTS devices. We provide clear evidence that the omnipresent cation disorder is not responsible for the large Urbach tails observed in many CZTS solar cells. In addition, the band-gap fluctuations due to cation disorder have a limited impact on the V_{OC} deficit. Instead, the V_{OC} deficit is largely accounted for by the deep centers associated with Sn antisite and its defect complexes, which proliferate in the presence of extensive cation disorder and impose the ultimate limit on the highest efficiency that can be achieved on CZTS devices.

Results

Cation disorder and band tailing

The CE formalism presents a rigorous statistical approach for sampling the configurational space.[19] Combined with Monte-Carlo (MC) simulations, the CE method is well suited for treating configurational disorder in solids.[20–26] Specifically, the CE method describes the configurational dependence of any scalar property Λ of a complex system through an effective model Hamiltonian characterized by the occupation vector $\boldsymbol{\sigma}$

$$\Lambda(\boldsymbol{\sigma}) = \sum_{\alpha} V_{\alpha} \Phi_{\alpha}(\boldsymbol{\sigma}), \qquad (1)$$

where the effective interaction V_{α} refers to the expansion coefficient of the cluster α, and the sum runs over the cluster correlation functions $\Phi(\boldsymbol{\sigma})$ of all symmetrically distinct clusters. The clusters are a subset of sites forming the lattice (*e.g.*, points, pairs, triplets, quadruplets, *etc.*). Once the specific property $\Lambda(\boldsymbol{\sigma})$ is known, the expansion coefficient V_{α} can be determined by the Connolly–Williams method.[27]

We consider stoichiometric CZTS and focus on the binary Cu–Zn disorder, as the Sn disorder is irrelevant at typical annealing temperatures ($<600\ °C$).[5,23] For the binary expansion, the cluster function is a simple product of occupation variables σ_i pertinent to the cluster α, *i.e.* $\Phi_{\alpha}(\boldsymbol{\sigma}) = \prod_{i \in \alpha} \sigma_i$. Here, σ_i takes either -1 if the site is occupied by Cu, or $+1$ if occupied by Zn. In addition to the empty and point clusters, we include the pair clusters up to the second-nearest neighbor (2NN) and the triplet cluster within the first-nearest neighbor (1NN) [*cf.* Fig. 1(a)].
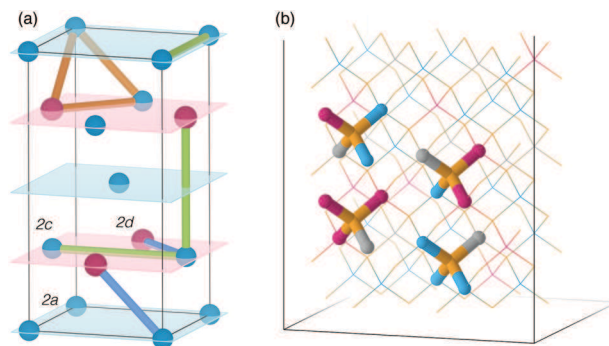

Fig. 1 (a) Clusters included for the CE. The pair 1NN, pair 2NN, and triplet 1NN clusters are shown in blue, green, and orange, respectively. The crystal structure depicted corresponds to the kesterite structure, and the Cu/Zn sites are labeled by the Wyckoff positions. Only the CE-active sites (Cu and Zn) are shown. (b) CZTS structure with extensive cation disorder highlighting the presence of the four S-centered tetrahedral motifs (Cu: blue; Zn: magenta; Sn: gray; S: orange).

Fig. 2(a) shows the occupancy of Cu obtained with canonical MC simulations using the effective cluster interactions fitted from the CE. Within the (001) plane, the Cu occupancy (at 2c and 2d)
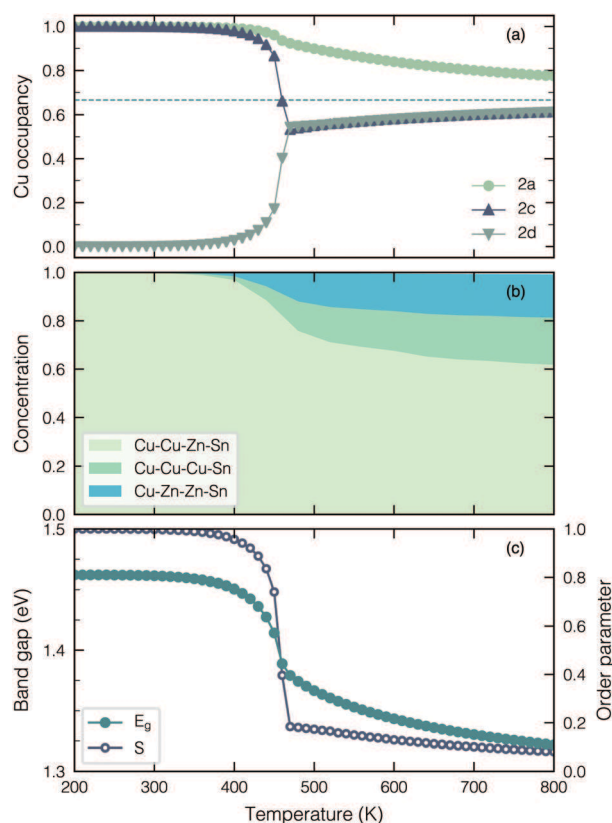

Fig. 2 Temperature dependence of (a) Cu occupancy at the three possible lattice sites, (b) concentration of various S-centered tetrahedral motifs, and (c) fundamental band gap (E_g) and long-range order parameter (S). Taking into account the band-gap underestimation, we apply a rigid shift of 0.9 eV to the PBE+U band gaps from the training set. The order parameter is calculated as $(P_{Cu} - 2/3)/(1 - 2/3)$, where P_{Cu} is the probability of Cu occupying the 2a and 2c sites.

3568 | *Energy Environ. Sci.*, 2021, **14**, 3567–3578

This journal is © The Royal Society of Chemistry 2021

changes sharply at the critical temperature T_C of 470 K, indicative of a second-order phase transition. The T_C is in good agreement with the experimental order–disorder transition temperature (533 ± 10 K) for CZTS.[28] Beyond T_C, the Cu occupancy within the (001) plane becomes degenerate towards the limit of a fully disordered occupancy (2/3). The Cu–Zn disorder is also present at the 2a site, but it is less significant than the plane disorder as a preference for Cu occupation has been observed.[23,29–31] As a consequence of the disorder, the stoichiometric Cu–Cu–Zn–Sn tetrahedral motif is not necessarily maintained [*cf.* Fig. 1(b)], in violation of the octet rule. The MC simulations show that about 40% of the tetrahedra become substoichiometric at high temperatures, half of which are Cu rich (Cu–Cu–Cu–Sn) and the rest Cu poor (Cu–Zn–Zn–Sn). The concentration of the Zn–Zn–Zn–Sn motif is negligible.

As the next step, we perform a CE of the band gaps based on the PBE+U results using ridge linear regression. The optimal hyperparameters are determined through a 5-fold cross-validation. We find that the band gap is well described by the CE with an RMSE of 0.06 eV. The fitted cluster expansion coefficients and the correlation functions obtained from the MC simulations are used to predict the temperature dependence of the band gap. The second-order transition in the band gap is clear from Fig. 2(c). Compared with the fully ordered kesterite, extensive Cu–Zn disorder is found to decrease the band gap by 130 meV as the order parameter approaches 0. For reference, various experiments reported a band-gap decrease of 40–200 meV due to disorder in CZTS(Se),[5,7–9] reasonably in line with our CE results.

To shed light on the origin of the disorder-induced band-gap decrease, we perform a CE of the density of states (DOS) $D(E)$. The procedure is similar to the CE of the total energy or the band gap except that it is carried out at a finite mesh of energy (E) and the expansion coefficients $V_\alpha(E)$ are now energy dependent. To account for the shift in the electrostatic potential due to the

Cu–Zn disorder, the semicore Cu-3p band is used as a reference for aligning the DOS of the training supercells. The predicted DOS values associated with the correlation functions at various temperatures are shown in Fig. 3(a). As expected, broadening is clearly visible for the valence band and the conduction band as the temperature elevates. Compared with the ordered kesterite, annealing at high temperatures beyond T_C leads to a rigid valence band maximum (VBM) shift of 0.1 eV towards the midgap. The conduction band minimum (CBM), by contrast, is nearly unperturbed because of its predominant Sn-5s character regardless of the Cu–Zn disorder. Therefore, we conclude that band-gap fluctuations in the presence of Cu–Zn disorder stem from the VBM fluctuations.

It is instructive to examine the expansion coefficients, *i.e.* the effective cluster DOS (ECDOS), for the states appearing above the VBM of kesterite. The ECDOS values per cluster function are given in Fig. 3(b)–(e). Whether a specific cluster enhances or weakens the DOS is determined by the product of the ECDOS and the corresponding cluster correlation function. For the point clusters, the negative ECDOS values thus ascribe the tail states near the VBM to the Cu sites. This is in agreement with the fact that the top of the valence band of CZTS consists mainly of Cu-3d states. Likewise, the positive ECDOS value for the NN-pair cluster suggests that either the Cu–Cu or the Zn–Zn pairs are at play, although the latter can be discarded in light of the negligible contribution of Zn atoms to the top of the valence band. The role of Cu is further supported by the NN-triplet cluster, for which the negative ECDOS values imply the importance of the Cu–Cu–Cu triplet cluster. A decomposition of the DOS into the respective cluster components shows that the Cu–Cu clustering is indeed the cause of the band-gap narrowing at high temperatures, as the development of the DOS above the VBM is largely attributed to the NN-pair and the NN-triplet clusters [*cf.* Fig. 3(b)–(e)].

The V_{OC} deficit in photovoltaic materials has been shown to correlate with the degree of band tailing.[32] For CZTSSe devices,
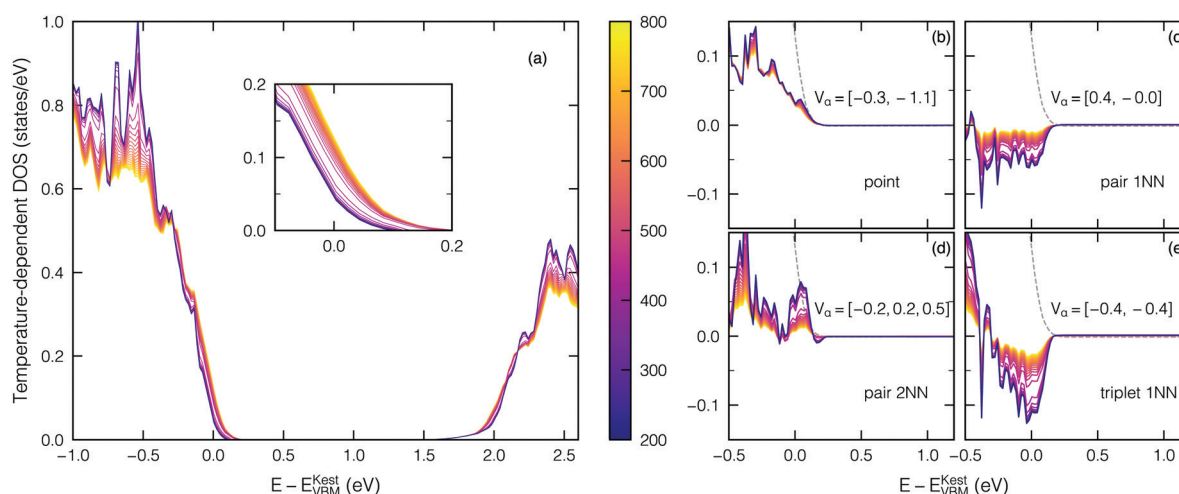

Fig. 3 (a) Dependence of DOS as a function of temperature. The energies are referred to the VBM of the kesterite. Only the configurational aspects of the temperature effects are taken into account. A rigid scissor shift of 0.9 eV to the conduction band is applied on top of the PBE+U results. The inset shows a zoom of the region near the VBM. (b)–(e) The cluster-resolved components of the DOS and the ECDOS (V_α in states/eV) per cluster function averaged over the energy window ranging from E_{VBM} to E_{VBM} + 0.2 eV. The temperature-independent contribution from the empty cluster is shown by the dashed lines.
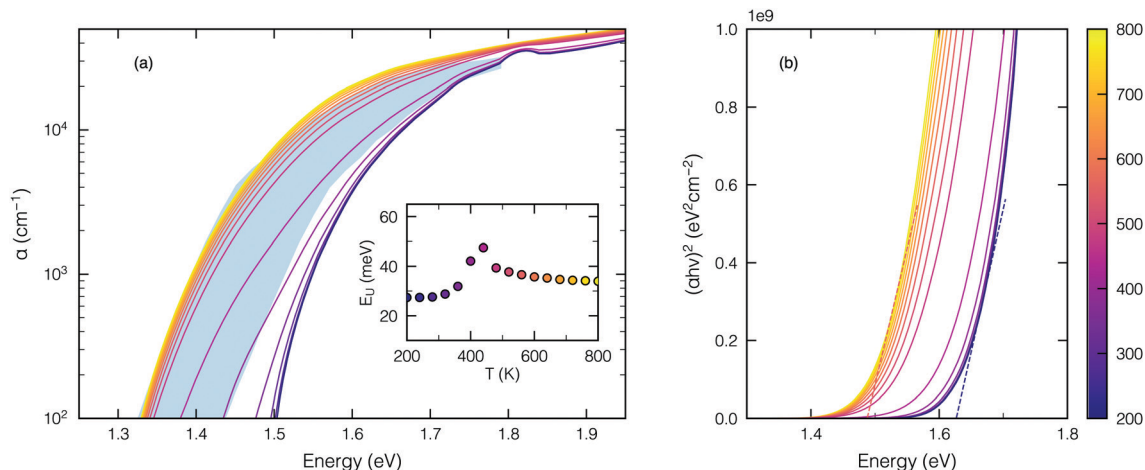
Fig. 4 (a) Optical absorption coefficient α and (b) Tauc plot as a function of temperature. In (a), the Urbach energies E_U extracted from the absorption coefficient are given in the inset. For reference, the photoluminescence (PL) absorption coefficient of CZTSSe[12] is shown in the shaded area where the boundaries correspond to the disordered and partially ordered samples. In (b), the experimental spectra are shifted to account for the difference between the experimental Tauc band gap of CZTSSe and the band gap determined from the Tauc plot.

a higher V_{OC} deficit is generally accompanied by a stronger band tailing and hence a larger Urbach energy.[5] To understand the effect of cation disorder on the band tailing, we carry out a CE of the optical absorption coefficient α. The absorption coefficient is calculated as

$$\alpha(\omega) = \frac{4\pi\omega}{c}\sqrt{\frac{\sqrt{\varepsilon_1^2(\omega) + \varepsilon_2^2(\omega)} - \varepsilon_1(\omega)}{2}}, \qquad (2)$$

where the dielectric function $\varepsilon = \varepsilon_1 + i\varepsilon_2$ is obtained within the independent-particle approximation for the training supercells. The band-gap narrowing is clearly visible in the predicted absorption coefficient [Fig. 4(a)] and in the Tauc plot [Fig. 4(b)] as the temperature increases. To enable a comparison with the experimental spectra of CZTSSe,[12] we shift the experimental optical absorption spectra to account for the difference between the experimental Tauc band gap of the disordered CZTSSe and the one determined from Fig. 4(b) at high temperature. The predicted absorption coefficients at high temperature agree remarkably well with experiment. At low temperature the discrepancy arises likely due to the fact that the reference CZTSSe is not absolutely free of cation disorder. We further estimate the Urbach energy E_U as the inverse of the the slope of $\ln(\alpha)$ for α ranging from 200 to 2000 cm^{-1}. For the ordered kesterite, we obtain an E_U of 30 meV. Interestingly, at high temperatures beyond the critical point of phase transition, our CE predicts that the E_U increases by no more than 10 meV [cf. the inset of Fig. 4(a)], thereby excluding the extensive Cu–Zn disorder as a major cause of the large band tailing in CZTS.

Point defects in disordered CZTS

Disorder-assisted defect stabilization. Except for some cation antisites and vacancies, the majority of point defects in CZTS are presumed insignificant because of their high formation energies.[33–35] Nevertheless, these assertions are drawn on the basis of dilute defect models in the otherwise perfectly ordered kesterite structure.

To understand to what extent the point defects are modified by the omnipresent Cu–Zn disorder, we generate a special 288-atom supercell for which the cluster correlation functions match closely the ones obtained with the MC simulations carried out at 800 K. The validity of the 288-atom supercell is manifested by the radial correlation functions, which agree well with those of MC simulations particularly up to the fourth shell (cf. Fig. S1, ESI†). PBE+U calculations show that the band gap of the special supercell is 0.2 eV smaller than that of the ordered kesterite, which is in agreement with the CE prediction (cf. Fig. 2). The more accurate Heyd–Scuseria–Ernzerhof (HSE) hybrid functional gives a band gap of 1.0 eV, compared with 1.4 eV for the ordered kesterite.

In the ordered kesterite where the stoichiometric Cu–Cu–Zn–Sn motif is formed everywhere, the cations contribute a nominal charge of +2, which is in balance with the −2 charge from the anion S. Such an octet rule is inevitably perturbed by the introduction of point defects, and the formation energy thus depends on the chemical environment near the defect which could either enhance or minimize the charge imbalance. To probe to what extent the defect formation energies are modified by the cation disorder, we consider all native vacancies and cation antisites embedded in the special supercell and evaluate their formation energy at the neutral charge state without taking into account structural relaxations. The formation energies are then compared with the ones obtained within an ordered supercell. We correlate the results with the tetrahedral environment surrounding the defect. Specifically, for defects involving the cations (Cu, Zn, and Sn), the defect site can be characterized by a feature set $\{n_i\}_{i=1}^4$ where n_i denotes the number of one specific tetrahedral motif in the immediate vicinity and $\sum n_i = 4$. For the S vacancy, we consider the tetrahedral motif in which the vacancy is encompassed. Fig. 5 shows that the defect formation energies can be well described by a linear model based on the feature set $\{n_i\}$, hence drawing a direct
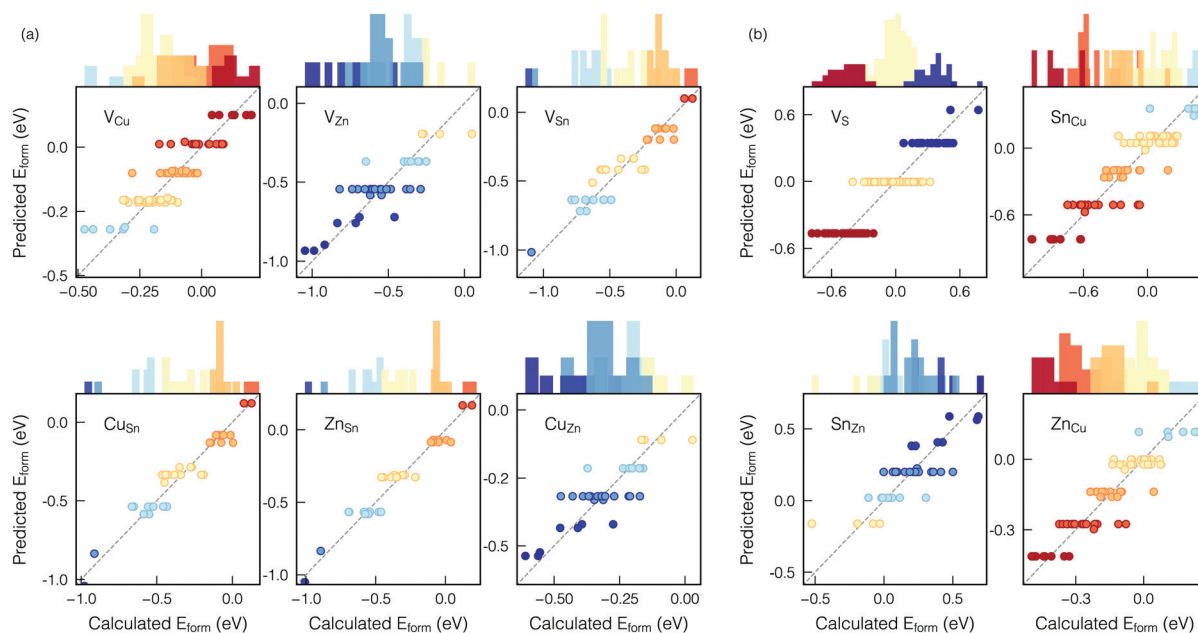
3570 | Energy Environ. Sci., 2021, 14, 3567–3578

This journal is © The Royal Society of Chemistry 2021

Fig. 5 Distribution of formation energies of acceptor-like (a) and donor-like (b) native defects in CZTS with extensive Cu–Zn disorder modeled by a special supercell obtained from MC simulations at 800 K. The formation energies are calculated for the neutral charge state with PBE+U excluding any structural relaxations, and are given in reference to the values obtained with perfectly ordered CZTS. The various sites at which a specific defect is located are characterized by its surrounding tetrahedral motifs, which are either Cu rich (red), Cu poor (blue), or stoichiometric (yellow). For the linear regression, formation energies are fitted to $E_0 + \alpha_i n_i$, where n_i is the number of one specific tetrahedral motif encompassing the defect site. L$_2$ regularization and 5-fold cross-validation are used to reduce overfitting.

correlation between the degree of defect stabilization and the local tetrahedral environment. In general, the acceptor-like defects are easier to form at the Cu-poor sites (Cu–Zn–Zn–Sn and Zn–Zn–Zn–Sn), whereas the donor-like defects are more populated at the lattice sites with excess Cu (Cu–Cu–Cu–Sn). Overall, we find that, in the presence of cation disorder, the formation energies can be lowered by 0.5 eV to 1 eV compared with the calculations carried out in a perfectly ordered supercell. This suggests that the defect concentrations in CZTS are markedly higher than earlier estimations without accounting for the cation disorder.

Defect levels and equilibrium concentrations in disordered CZTS. Having identified the energetically favorable sites for the formation of defects, we focus on the defect formation energies at such sites, as they dictate the thermal equilibrium of defects and charge carriers. To this end, we perform full HSE hybrid-functional calculations on the lowest-energy defect sites and calculate the associated defect formation energies in cation-disordered CZTS. The formation energies and the ensuing thermodynamic charge transition levels are shown in Fig. 6 for the acceptors and donors of the lowest formation energy, together with the results obtained in ordered CZTS for comparison. The magnitudes of stabilization as a result of cation disorder are found to be in good agreement with those predicted in Fig. 5. We further assess the defect concentrations in thermal equilibrium using the charge neutrality condition $p_0 - n_0 + \sum q N(D^q) = 0$, where p_0 (n_0) is the thermal hole (electron) concentration at room temperature, and $N(D^q)$ is the defect concentration for charge state q at the typical synthesis temperature of 800 K. We assume that the defects generated at high temperatures are
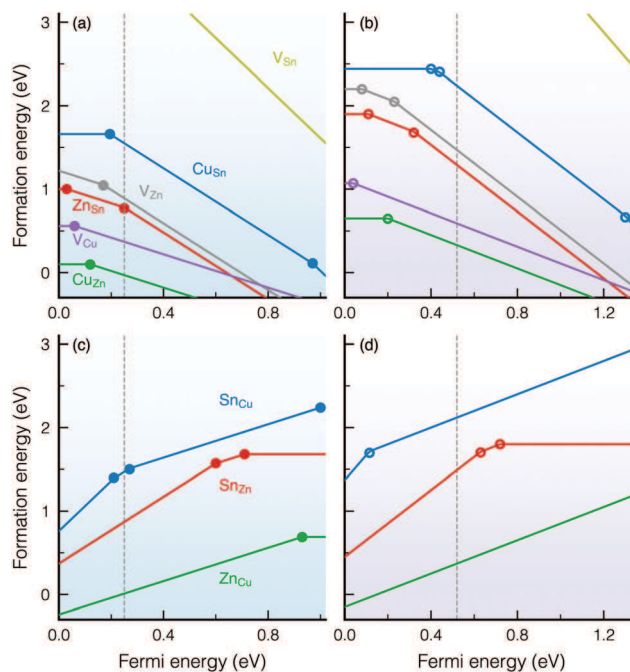

Fig. 6 Calculated formation energies of (a) acceptors and (c) donors in the disordered CZTS using the HSE hybrid functional. The corresponding results in the ordered CZTS are shown in (b) and (d) for acceptors and donors, respectively. The Fermi energy is referred to the VBM. The equilibrium Fermi level at 300 K is shown by the dashed vertical line. We consider the Cu-poor and Zn-rich conditions for the growth of stoichiometric CZTS ($\Delta\mu_{Cu}$ = −0.50 eV, $\Delta\mu_{Zn}$ = −1.54 eV, $\Delta\mu_{Sn}$ = −0.57 eV).

This journal is © The Royal Society of Chemistry 2021

Energy Environ. Sci., 2021, **14**, 3567–3578 | **3571**

frozen in during cooling. For illustrative purposes, we focus on the Cu-poor and Zn-rich growth conditions which are commonly used for achieving high-performance CZTS devices.[3] A more complete account under various growth conditions is provided in the ESI.†

In cation disordered CZTS, Cu_{Zn} and V_{Cu} maintain the lowest formation energies among the acceptors, and thus remain the main sources of p-type conductivity with shallow ($-/0$) acceptor levels at E_{VBM} + 0.12 eV and E_{VBM} + 0.06 eV. Among the donors, we find that Zn_{Cu} is the most important compensating defect with a shallow donor level ($0/+$) appearing at E_{CBM} − 0.08 eV. We note that Cu and Zn interstitial defects have also been predicted as shallow donors in CZTS, but they have considerably higher formation energies than Zn_{Cu}.[33] In thermal equilibrium, the Fermi level is therefore mainly determined by the compensation among the acceptors Cu_{Zn} and V_{Cu} and the donor defect Zn_{Cu}. Under the specific Cu-poor and Zn-rich growth conditions, our calculations position the equilibrium Fermi level at E_{VBM} + 0.25 eV, in comparison with E_{VBM} + 0.52 eV as obtained with the ordered CZTS. The lowered Fermi level, as a result of the stronger defect stabilization for the shallow acceptors, suggests that the presence of cation disorder could significantly increase the hole concentration (cf. Table 1). Indeed, Rey et al. observed that the free carrier concentration for disordered CZTSe is an order of magnitude higher than for more ordered CZTSe.[13]

In view of the lower defect formation energies and the lower equilibrium Fermi level, the defect concentrations in thermal equilibrium are typically 10 to 10^4 times higher in the presence of extensive Cu–Zn disorder (cf. Table 1). Sn_{Zn} and Sn_{Cu} are the two most important deep donors in CZTS, for which the deep donor levels are associated with the high ionization energy of the Sn-5s state. These two donors are significantly more populated in disordered CZTS. At an estimated density of 10^{16} cm^{-3} under the

Cu-poor and Zn-rich conditions, the role of Sn_{Zn} as a recombination center is further substantiated. The large electron capture cross section of Sn_{Zn} has been recently confirmed by two theoretical studies.[36,37] It is established that the large capture cross section of Sn_{Zn} is facilitated by the large lattice distortion upon electron capture at the Sn site, showing the elongated Sn–S bonds by about 0.1 Å. We find that such a large lattice distortion is also present in disordered CZTS. Together with the deep charge transition levels close to the midgap, we conclude that Sn_{Zn} remains an effective recombination center in the presence of cation disorder.

Due to the similar Sn chemistry, the large lattice distortions are also present with Sn_{Cu} upon charging. The average Sn–S bond length increases by 0.14 Å as Sn_{Cu}^{3+} reduces to Sn_{Cu}^{2+}, and further by 0.13 Å as Sn_{Cu}^{2+} reduces to Sn_{Cu}^{1+}. Analogous to Sn_{Zn}, the large distortion could lead to a lowered electron capture barrier for Sn_{Cu}^{3+} and Sn_{Cu}^{2+}, but as the donor levels of Sn_{Cu} are near the VBM and away from the midgap, the role of Sn_{Cu} in nonradiative recombination can be much limited in comparison with Sn_{Zn}.

On top of isolated point defects, the quaternary kesterite hosts a number of defect complexes, the formation energy of which can be much lower compared with the sum of the isolated ones. Indeed, the self-compensated donor–acceptor pair Zn_{Cu} + Cu_{Zn} is predicted to be of the lowest formation energy among all native defects regardless of growth conditions.[33] Meanwhile, our model of Cu–Zn disorder already implies the ubiquitous occurrence of Zn_{Cu} + Cu_{Zn}, which, as an antisite pair, would then form spontaneously in the presence of cation disorder. The other two stoichiometry-preserving antisite pairs, i.e. Sn_{Cu} + Cu_{Sn} and Sn_{Zn} + Zn_{Sn}, are energetically less favorable in either disordered or ordered CZTS as indicated by Fig. 7(a) and (b). More distinct from Zn_{Cu} + Cu_{Zn}, the localized nature of Sn antisites leads to deep defect levels within the band gap. This is in particular the case for Sn_{Cu} + Cu_{Sn} in ordered CZTS, as the amphoteric defect complex shows a deep donor level and two deep acceptor levels. Nevertheless, the effect of Sn_{Cu} + Cu_{Sn} and Sn_{Zn} + Zn_{Sn} is minimal given the low defect concentration in ordered CZTS and the fact that these deep levels move away from the midgap as the band gap shrinks due to cation disorder. In fact, we predict that all cation antisite pairs remain largely neutral at Fermi levels throughout the band gap in disordered CZTS.

Among the non-stoichiometric defect complexes, Sn_{Zn} + $2Cu_{Zn}$ bears the lowest formation energy. Note that the present HSE calculations place the formation energy about 1 eV higher than that obtained with semilocal DFT.[33,38] It is only when cation disorder is taken into account that the formation energy of Sn_{Zn} + $2Cu_{Zn}$ reduces to 0.5 eV under Zn-rich conditions and even tends to zero under Zn-poor conditions. In addition, Sn_{Zn} + $2Cu_{Zn}$ produces two deep acceptor levels pertinent to the (double) reduction of the ionized donor Sn_{Zn}^{2+}. These deep acceptor levels, characteristic of other self-compensated Sn_{Zn} defect complexes, could serve as electron trapping centers. At sufficiently high concentrations (e.g. under Zn-poor conditions), the acceptor levels associated with Sn_{Zn} + $2Cu_{Zn}$ may eventually broaden and form band tails near the CBM.[39] When Sn_{Zn} binds to one

Table 1 Thermal equilibrium defect concentration N and hole concentration p_0 at equilibrium Fermi energy E_F in cation disordered and ordered CZTS. The defect concentration corresponds to the sum over all relevant charge states. A detailed breakdown of defect concentrations for various charge states can be found in Table S1 of the ESI. The results assume the same growth conditions as given in Fig. 6

	Cation disordered	Ordered
E_F (eV)	0.25	0.52
p_0 (cm^{-3})	1×10^{15}	3×10^{10}
N (cm^{-3})		
V_{Cu}	4×10^{19}	2×10^{18}
Cu_{Zn}	9×10^{21}	5×10^{19}
Zn_{Sn}	1×10^{17}	5×10^{13}
V_{Zn}	1×10^{16}	4×10^{12}
Cu_{Sn}	1×10^{12}	7×10^7
V_{Sn}	4×10^{-1}	2×10^{-4}
Zn_{Cu}	8×10^{21}	6×10^{19}
Sn_{Cu}	9×10^{12}	5×10^8
Sn_{Zn}	1×10^{16}	2×10^{12}
Sn_{Cu} + Cu_{Sn}	8×10^{11}	5×10^3
Sn_{Zn} + Zn_{Sn}	2×10^{16}	1×10^{13}
Sn_{Zn} + V_{Zn}	4×10^{15}	1×10^8
Sn_{Zn} + $2V_{Cu}$	2×10^{14}	7×10^{10}
Sn_{Zn} + $2Cu_{Zn}$	4×10^{18}	6×10^{12}
Sn_{Zn} + Cu_{Zn}	3×10^{16}	1×10^{13}

3572 | Energy Environ. Sci., 2021, **14**, 3567–3578

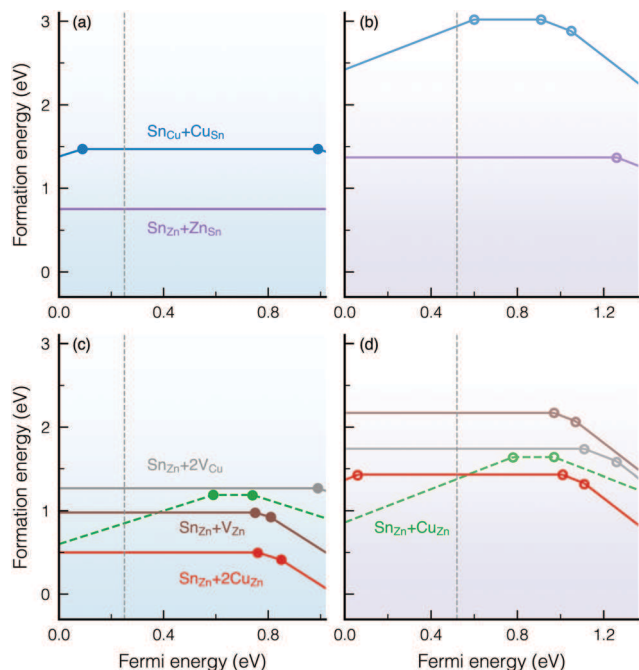This journal is © The Royal Society of Chemistry 2021

Fig. 7 Formation energies of (a) stoichiometric and (c) non-stoichiometric donor−acceptor pairs in the disordered CZTS and in the ordered CZTS (b and d). The notions and growth conditions follow those of Fig. 6.

neighboring Cu_{Zn} to form a less charge compensated defect complex, the possibility to either reduce or oxidize the Sn_{Zn}^{1+} gives rise to a deep acceptor level in addition to a deep donor level near the midgap [*cf.* Fig. 7(c) and (d)]. Electrically, the deep donor level of $Sn_{Zn} + Cu_{Zn}$ is close to that of the isolated Sn_{Zn}, but its lower formation makes the defect complex more relevant in nonradiative recombination, particularly under Cu-rich and Zn-poor conditions (*cf.* Fig. S4, ESI†).

One remaining question pertinent to the band tails is whether extensive cation disorder by itself could stabilize self-trapped electrons or holes by small-polaron formation. The self-trapping is observed or predicted in some structurally disordered systems, such as in amorphous SiO_2[40] and disordered HfO_2.[41] Nonetheless, our calculations show no signs of electron or hole polarons due to cation disorder in CZTS.

Discussion

Band-gap fluctuations

Our results indicate that extensive Cu–Zn disorder *per se* does not necessarily account for the stronger Urbach tails in stoichiometric CZTS. This is consistent with recent photoluminescence measurements showing a constant Urbach energy as the degree of cation disorder varies.[12] The insensitivity of Urbach tails to cation disorder is not unexpected since the compensated defect pair $Zn_{Cu} + Cu_{Zn}$ does not produce any localized defect state in the band gap.

The Urbach energy of 30 meV obtained with the present study is in agreement with the recent experimental values extracted from PL spectra for a number of CZTSSe and CZTSe samples of various degrees of Cu–Zn order.[12] The relatively

large Urbach energy compared with other solar absorbers (*e.g.* Si and GaAs) arises from the nonparabolicity of the valence-band edge of ordered CZTS.[42] It is noteworthy that the Urbach energy of 30 meV is also characteristic of other thin-film absorbers such as CuInGaSe (CIGS),[32] yet the V_{OC} deficit of CZTSSe is markedly higher (by over 100 meV).[5] Therefore, the large V_{OC} cannot be interpreted by the band tails alone.

While Cu–Zn disorder does not affect the Urbach tails, it reduces the band gap by forming the valence-band tails through Cu clustering. The valence-band tails, which are of an extended nature, are sometimes referred to as the Gaussian tails[43] because of the Gaussian fluctuations of the band gap. These tail states do not contribute to the Urbach tails but lead to a redshift of the optical absorption onset as evidenced by the experimental absorption spectra.[12]

In disordered systems, the reduced band gap originates from the spatial fluctuations of the band gap. To visualize the extent of the band-gap fluctuations, we calculate for the special supercell the local electronic density of states values, which are averaged along the [001] direction as shown in Fig. 8. The band-gap fluctuations are clearly visible for the disordered CZTS, with the VBM undergoing an upward shift where excess local Cu–Cu–Cu–Sn tetrahedra are formed. The valence-band fluctuations thus result from the compositional inhomogeneity due to cation disorder. A similar observation was made by Zawadzki *et al.* that Cu-rich motifs tend to raise the VBM of CZTS, the origin of which was assigned to the localized negative electrostatic potential affecting the Cu-d states.[44] At variance, the conduction-band edges are hardly
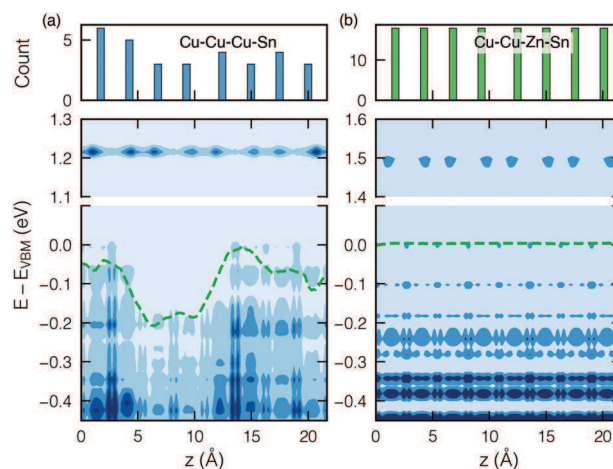

Fig. 8 Planar-averaged local electronic density of states for (a) disordered and (b) ordered CZTS calculated with PBE+U. The energy levels are referred to the VBM. The spatially resolved valence-band edge is highlighted by the green dashed isoline of the local DOS. The isovalue is chosen so that the the isoline at the highest energy reconciles the VBM. Specifically, the isovalue corresponds to 4×10^{-4} and 1×10^{-5} states/eV Å^2 for the disordered and the ordered CZTS, respectively. A macroscopic planar average of the isoline is further carried out over the size of a unit cell (5.4 Å). The CBM is shifted rigidly to account for the band-gap underestimation. For the disordered CZTS, a histogram depicting the number of the Cu-rich motif Cu–Cu–Cu–Sn is shown on the top panel. The ordered CZTS is characterized by a uniform distribution of the Cu–Cu–Zn–Sn motif.

This journal is © The Royal Society of Chemistry 2021

Energy Environ. Sci., 2021, **14**, 3567–3578 | **3573**

perturbed by the local composition as is expected from the CE analysis. According to Rau *et al.*, the band-gap fluctuations contribute to the V_{OC} deficit by $\sigma_g^2 q/2k_B T$,[45] where σ_g is the standard deviation of the band gap, and q the elementary charge. Using $\sigma_g = 60$ meV as extracted from Fig. 8(a), we estimate that, as the result of Cu–Zn disorder, band-gap fluctuations lead to the V_{OC} deficit of 70 meV at room temperature, hence leaving the majority (nearly 90%) of the V_{OC} deficit unaccounted for.

Nonradiative recombinations in disordered CZTS

Deep centers, on the other hand, can be detrimental to photovoltaic efficiency in that they enhance the nonradiative dark saturation current, thereby reducing the quantum efficiency and the V_{OC}.[46,47] Our study identifies Sn_{Zn} and $Sn_{Zn} + Cu_{Zn}$ as the lowest-energy deep donors that are most likely to be responsible for nonradiative recombination. This is in agreement with previous theoretical work.[38,48] However, our work points out that the Cu–Zn cation disorder is necessary to stabilize these defects to concentration levels where they start to be actually detrimental. The stabilization is partly assisted by a shift of the Fermi level towards the VBM under equilibrium. More quantitatively and based on the Schockley–Read–Hall (SRH) model,[49,50] we assess the nonradiative recombination lifetime for the two predominant deep donors, *i.e.* Sn_{Zn} and $Sn_{Zn} + Cu_{Zn}$, under Cu-poor and Zn-rich growth conditions. We provide in Table 2 the minority carrier lifetime with and without disorder. The effect of disorder is dramatic, with lifetime being reduced by several orders of magnitude. Our lifetime estimate of around 1 ns agrees reasonably well with experimental reports,[51] albeit only when cation disorder is taken into account. We also compute in Table 2 a maximum conversion efficiency (*i.e.*, assuming the only detrimental processes are due to SRH recombination). If disorder is taken into account, the maximum efficiency drops from 25% to 14%. This is compared with the record efficiency of CZTS devices standing at 11%.[52] We note that, recently, a similar estimate of the SRH limited efficiency by Kim *et al.* has given a much more optimistic value of 20% but assuming an ordered kesterite.[48] Our work suggests that the conversion efficiency achieved experimentally in disordered CZTS might be already close to its theoretical limit.

Apart from the deleterious nonradiative recombination, minority carrier trapping due to $Sn_{Zn} + 2Cu_{Zn}$ could also be problematic. In particular for Zn-poor growth conditions, the high concentration of $Sn_{Zn} + 2Cu_{Zn}$ could eventually lead to the formation of conduction-band tail states. The localized tail states associated with Sn_{Zn} are likely at the origin of the large Urbach tails observed with many CZTS solar cells.[39,43]

At first sight, the effect of disorder on deep defects we uncovered might motivate further work on the minimization of cation disorder. However, experimental evidence shows that long-range order parameter hardly exceeds 0.8 at room temperature due to the extremely slow ordering process at finite temperatures.[8,16] According to Fig. 2(b), at $S = 0.8$ about 20% of the tetrahedra would be substoichiometric, compared with the fraction of 40% when $S = 0.1$. This suggests that defect proliferation seen in the highly disordered CZTS should also occur at a relatively low degree of disorder, and as such, the role of recombination and trapping centers remain important irrespective of the thermal treatment. This could explain why efforts in reducing disorder have not been effective in reducing the V_{OC} deficit. For instance, Bourdais *et al.* noted that the V_{OC} improves by only 40 meV for CZTSSe samples treated with slow cooling compared with those of higher disorder.[5] Larsen *et al.* also found that the V_{OC} deficit of CZTS is not necessarily reduced as the ordering improves.[14,15]

Our results suggest that a more viable route towards higher V_{OC} is by suppressing the formation of deep centers pertinent to the Sn_{Zn} antisites through optimal growth conditions. In addition to the common practice that Zn-poor conditions are to be avoided, this can be achieved under Sn-poor or S-rich conditions without compromising the p-type conductivity (*cf.* Fig. S4, ESI†). Experimentally the Sn-poor composition is found effective in reducing band tailing and deep donor defects,[39] whereas an improved V_{OC} is obtained under a high sulfur partial pressure during non-equilibrium annealing at high temperature.[53] Nonetheless, because of the narrow phase stability (*cf.* Fig. S1, ESI†) and the restricting Cu-poor growth conditions, the concentration of Sn antisites cannot be significantly reduced without the formation of secondary phases (*cf.* Table S1, ESI†).

In recent years, the stagnated improvement in the efficiency of CZTSSe has prompted the practice of cationic substitution in order to overcome the large V_{OC} deficit.[3] The strategy is either to reduce the cation disorder (*e.g.* by substituting Cu with Ag,[54–59] and Zn with Cd[59–63]), or to eliminate the Sn-related deep centers (*e.g.* by substituting Sn with Ge[64–67]). The issues concerning the toxicity of Cd and the rarity of Ge can be mitigated by partial substitution and alloying. Cationic substitution has been very successful in enhancing V_{OC} and reducing band tailing. For instance, the recent Cd-alloyed CZTS shows an efficiency of over 12%[63] compared with the record efficiency (11%) of pure CZTS. Among other factors including improved band alignment and interface properties, our results hint at the importance of disorder-induced defect stabilization in achieving the high efficiency. In particular, the lack of a second-order phase transition leads to a much smoother order–disorder transition for Cu_2CdSnS_4 compared with CZTS,[24] which enables a higher degree of ordering and thus could suppress the formation of nonradiative recombination centers. The methodology outlined in our work hence offers an avenue to accessing the atomistic origin of the improved efficiency for these emerging CZTS-derived solar absorbers.

Looking forward, we envisage an extension to the present work where cation disorder and point defects are treated on the

Table 2 Nonradiative recombination lifetime τ for Sn_{Zn}^{2+} and $[Sn_{Zn} + Cu_{Zn}]^+$ assessed in ordered and disordered CZTS under Cu-poor and Zn-rich growth conditions. The trap-limited conversion efficiency η is estimated based on the two predominant Sn_{Zn}-related deep donors

	Cation disordered		Ordered	
	Sn_{Zn}^{2+}	$[Sn_{Zn} + Cu_{Zn}]^+$	Sn_{Zn}^{2+}	$[Sn_{Zn} + Cu_{Zn}]^+$
τ (ns)	3.2	1.0	2.0×10^4	3.2×10^3
η (%)		14		25

same footing in the cluster expansion within a grand or semi-grand canonical ensemble. In fact, CZTS devices exhibit higher efficiencies with non-stoichiometric absorber layers, which are typically Cu-poor and Zn-rich.[68] The non-stoichiometry is generally accompanied by a large number of point defects or defect complexes, which could play a role in the order–disorder transition. Ultimately, the efficiency of kesterite solar absorbers is contingent upon the interplay between disorder and defects, the effect of which needs further investigation.

Conclusions

By a statistical treatment of the Cu–Zn disorder in CZTS using the cluster-expansion method, we show that extensive cation disorder barely modifies the band tailing as is characterized by the Urbach energy of 30 meV for both ordered and disordered CZTS. Local Cu clusterings due to cation disorder shift the VBM position, thereby leading to the spatial fluctuations of the valence-band edge and effectively reducing the band gap. Nevertheless, the band-gap fluctuations contribute only marginally to the V_{OC} deficit. While the omnipresent Cu–Zn disorder is not directly responsible for the low V_{OC} of the kesterite absorber, the extensive disorder stabilizes the formation of defects, among which the Sn_{Zn} antisite and its defect complexes are particularly detrimental to the V_{OC} through the mechanisms of nonradiative recombination and minority carrier trapping. Indeed, we show that the very short carrier lifetime and the low conversion efficiency observed experimentally for CZTS can be well accounted for by the Sn_{Zn}-related defects if the effect of cation disorder is fully taken into account. The persistence of such defects, even for a low degree of cation disorder, presents the major challenge towards high-efficiency kesterite solar cells.

Methods section

Stoichiometric and symmetrically distinct configurations comprising up to 24 atoms are enumerated using the CASM code.[69–72] Density-functional theory (DFT) calculations on these resulting 72 supercells are carried out with the semilocal Perdew–Burke–Ernzerhof (PBE) functional using the VASP simulation package.[73,74] For Cu, an additional Hubbard U of 6 eV is applied to the 3d electrons. A Γ-centered k-point mesh with a density of 12 000 k points per atom is used for Brillouin-zone sampling for total-energy calculations. The k-point mesh density is further increased to 12 000 per atom for optical absorption calculations. MC simulations are carried out in a canonical ensemble using a 20 × 20 × 20 supercell (64 000 atoms). At each temperature, 20 000 equilibration steps are performed followed by 40 000 production steps.

Defect calculations are carried out in a 288-atom special supercell mimicking the Cu–Zn disorder of CZTS at 800 K. To describe properly the electronic structure of CZTS and the charge localization of polarons, the standard Heyd–Scuseria–Ernzerhof (HSE) hybrid functional is used. The HSE calculations are performed with QUANTUM ESPRESSO[75–78] and the Pseudo-Dojo optimized norm-conserving pseudopotentials.[79–81] The single

Γ point is used for k-point sampling. Spin polarization is taken into account when necessary. The lattice parameters are kept fixed to the experimental values during structural relaxations.

The formation energy of a defect D^q at charge state q is given by

$$\Delta E_{form}^{[D^q]} = E_{tot}^{[D^q]} - E_{tot}^{bulk} - \sum_i n_i \mu_i + q E_F + E_{corr}, \qquad (3)$$

where $E_{tot}^{[D^q]}$ and E_{tot}^{bulk} are the total energies of the defect and the pristine supercell, respectively. The sum refers to the total chemical potentials μ of the n_i atoms added to (or removed from) the supercell. E_F is the Fermi level. Finite-size effects due to spurious electrostatic interactions in the periodic conditions are taken into account by E_{corr} using the scheme of Freysoldt and coworkers.[82–84]

The defect concentration at a given Fermi level is given by

$$N(D^q) = N_s e^{-\Delta E_{form}^{[D^q]}/k_B T}, \qquad (4)$$

where N_s is the number of sites (per unit volume) available to the defect. The concentrations for holes and electrons are given by

$$\begin{aligned} p_0 &= N_V e^{-(E_F - E_V)/k_B T} \\ n_0 &= N_C e^{-(E_C - E_F)/k_B T}, \end{aligned} \qquad (5)$$

where the effective density of states N_V of the valence band and $N + C$ of the conduction band can be determined from the corresponding effective masses $m_e^\star$ and $m_h^\star$

$$N_{C,V} = 2\left(\frac{2\pi m_{e,h}^* k_B T}{h^2}\right)^{3/2}. \qquad (6)$$

Here we use $m_e^\star = 0.17 m_0$ and $m_h^\star = 0.71 m_0$. The equilibrium Fermi level and concentrations of free carriers and charged defects can be determined via the charge neutrality condition

$$p_0 - n_0 + \sum q N(D^q) = 0. \qquad (7)$$

The nonradiative recombination lifetime is estimated using the Shockley–Read–Hall (SRH) model, which describes the recombination rate for an electron–hole pair through a trapping state within the band gap.[49,50] The recombination rate R_t associated with a single trapping state t is given by

$$R_t = \frac{np - n_0 p_0}{\tau_n [n + N_C e^{(E_t - E_C)/k_B T}] + \tau_p [p + N_V e^{(E_V - E_t)/k_B T}]}, \qquad (8)$$

where $n = n_0 + \Delta n$ and $p = p_0 + \Delta p$ denote the steady-state concentrations of electrons and holes, respectively. Here the electron and hole densities generated upon illumination are set to $\Delta n = \Delta p = 10^{14}$ cm^{-3}, a typical value for CZTS.[37] τ_n and τ_p in eqn (8) can be expressed by

$$\tau_{n,p} = (N_t C_{n,p})^{-1} = (N_t \sigma_{n,p} \nu_{n,p}^{th})^{-1}, \qquad (9)$$

where $\nu_{n,p}^{th}$ is the thermal velocity at 10^7 cm s^{-1}. For electron-capture cross sections we use $\sigma_n = 1.2 \times 10^{-14}$ cm^2 for Sn_{Zn}^{2+}[85] and $\sigma_n = 1.5 \times 10^{-13}$ cm^2 for $[Sn_{Zn} + Cu_{Zn}]^+$.[48] The hole-capture cross section is fixed at $\sigma_p = 3.2 \times 10^{-15}$ cm^2. The SRH process

This journal is © The Royal Society of Chemistry 2021

Energy Environ. Sci., 2021, **14**, 3567–3578 | **3575**

of the p-type CZTS is determined by the excess electron density Δn. As such, the minority carrier lifetime τ_n is given by

$$\tau_n = \frac{\Delta n}{R_{SRH}}, \tag{10}$$

where the total recombination rate R_{SRH} sums over the contributions from Sn_{Zn} and $Sn_{Zn} + Cu_{Zn}$.

Following the work of Krichartz and Rau,[86] the upper limit of power conversion efficiency is determined by

$$\eta = \frac{(JV)_{max}}{\int_0^\infty E\phi_{sun}(E)\mathrm{d}E}, \tag{11}$$

where J is the current density, V the voltage across the cell, and $\phi_{sun}(E)$ the photon number density of the solar AM1.5 spectrum at the energy E. The net current density takes into account both radiative and nonradiative recombinations

$$J = J_{SC} - J_{rad} - J_{SRH}, \tag{12}$$

where the terms on the right-hand side of the equation refer to the short-circuit current density under illumination, the current density limited by radiative recombination, and the current density due to the nonradiative recombination. The short-circuit current density generated under illumination is calculated as

$$J_{SC} = q \int_{E_g}^\infty \phi_{sun}(E)\left[1 - \mathrm{e}^{-2\alpha(E) \cdot d}\right]\mathrm{d}E, \tag{13}$$

where q is the elementary charge and d the thickness of the absorber layer. The radiative current density can be estimated by

$$J_{rad} = J_{rad}^0(\mathrm{e}^{qV/k_BT} - 1), \tag{14}$$

where the radiative saturation current density J_{rad}^0 is associated with the black-body radiation $\phi_{rad}(E)$ (at 300 K) as

$$J_{rad}^0 = q \int_{E_g}^\infty \phi_{rad}(E)\left[1 - \mathrm{e}^{-2\alpha(E) \cdot d}\right]\mathrm{d}E. \tag{15}$$

For the nonradiative current, two limiting cases are considered. Under the low-level injection conditions where one type of carrier is in excess (*i.e.*, when $p_0/n_0 \geq 100$), the nonradiative current density is given by

$$J_{SRH}^{low} = J_{SRH}^{low,0}(\mathrm{e}^{qV/k_BT} - 1), \tag{16}$$

and the nonradiative saturation current density is

$$J_{SRH}^{low,0} = \frac{qdN_CN_V}{p_0\tau}\mathrm{e}^{-E_g/k_BT}. \tag{17}$$

Under the high-level injection conditions where the electron and hole concentrations are comparable, the nonradiative current density can be expressed as

$$J_{SRH}^{high} = J_{SRH}^{high,0}(\mathrm{e}^{qV/2k_BT} - 1), \tag{18}$$

$$J_{SRH}^{high,0} = \frac{qd\sqrt{N_CN_V}}{2\tau}\mathrm{e}^{-E_g/2k_BT}. \tag{19}$$

Conflicts of interest

The authors declare no conflict of interest.

Acknowledgements

References

1 K. Ito and T. Nakazawa, *Jpn. J. Appl. Phys.*, 1988, **27**, 2094–2097.

2 S. K. Wallace, D. B. Mitzi and A. Walsh, *ACS Energy Lett.*, 2017, **2**, 776–779.

3 S. Giraldo, Z. Jehl, M. Placidi, V. Izquierdo-Roca, A. Pérez-Rodríguez and E. Saucedo, *Adv. Mater.*, 2019, **0**, 1806692.

4 W. Wang, M. T. Winkler, O. Gunawan, T. Gokmen, T. K. Todorov, Y. Zhu and D. B. Mitzi, *Adv. Energy Mater.*, 2014, **4**, 1301465.

5 S. Bourdais, C. Choné, B. Delatouche, A. Jacob, G. Larramona, C. Moisan, A. Lafond, F. Donatini, G. Rey, S. Siebentritt, A. Walsh and G. Dennler, *Adv. Energy Mater.*, 2016, **6**, 1502276.

6 S. Siebentritt, *Nat. Energy*, 2017, **2**, 840–841.

7 M. Valentini, C. Malerba, F. Menchini, D. Tedeschi, A. Polimeni, M. Capizzi and A. Mittiga, *Appl. Phys. Lett.*, 2016, **108**, 211909.

8 J. J. S. Scragg, J. K. Larsen, M. Kumar, C. Persson, J. Sendler, S. Siebentritt and C. Platzer Björkman, *Phys. Status Solidi B*, 2016, **253**, 247–254.

9 G. Rey, A. Redinger, J. Sendler, T. P. Weiss, M. Thevenin, M. Guennou, B. El Adib and S. Siebentritt, *Appl. Phys. Lett.*, 2014, **105**, 112106.

10 M. Nishiwaki, K. Nagaya, M. Kato, S. Fujimoto, H. Tampo, T. Miyadera, M. Chikamatsu, H. Shibata and H. Fujiwara, *Phys. Rev. Mater.*, 2018, **2**, 085404.

11 M. Lang, T. Renz, A. Opolka, C. Zimmermann, C. Krämmer, M. Neuwirth, H. Kalt and M. Hetterich, *Appl. Phys. Lett.*, 2018, **113**, 033901.

12 G. Rey, G. Larramona, S. Bourdais, C. Choné, B. Delatouche, A. Jacob, G. Dennler and S. Siebentritt, *Sol. Energy Mater. Sol. Cells*, 2018, **179**, 142–151.

13 G. Rey, T. Weiss, J. Sendler, A. Finger, C. Spindler, F. Werner, M. Melchiorre, M. Hála, M. Guennou and S. Siebentritt, *Sol. Energy Mater. Sol. Cells*, 2016, **151**, 131–138.

14 J. K. Larsen, F. Larsson, T. Törndahl, N. Saini, L. Riekehr, Y. Ren, A. Biswal, D. Hauschild, L. Weinhardt, C. Heske and C. Platzer-Björkman, *Adv. Energy Mater.*, 2019, **9**, 1900439.

15 J. K. Larsen, J. J. S. Scragg, N. Ross and C. Platzer-Björkman, *ACS Appl. Energy Mater.*, 2020, **3**, 7520–7526.

16 K. Rudisch, Y. Ren, C. Platzer-Björkman and J. Scragg, *Appl. Phys. Lett.*, 2016, **108**, 231902.

17 S. Schorr, H.-J. Hoebler and M. Tovar, *Eur. J. Mineral.*, 2007, **19**, 65–73.

3576 | *Energy Environ. Sci.*, 2021, **14**, 3567–3578

This journal is © The Royal Society of Chemistry 2021

18 D. M. Többens, G. Gurieva, S. Levcenko, T. Unold and S. Schorr, *Phys. Status Solidi B*, 2016, **253**, 1890–1897.

19 J. Sanchez, F. Ducastelle and D. Gratias, *Phys. A*, 1984, **128**, 334–350.

20 R. Magri, S. Froyen and A. Zunger, *Phys. Rev. B: Condens. Matter Mater. Phys.*, 1991, **44**, 7947–7964.

21 B. P. Burton, S. Demers and A. van de Walle, *J. Appl. Phys.*, 2011, **110**, 023507.

22 K. Yu and E. A. Carter, *Chem. Mater.*, 2016, **28**, 864–869.

23 S. P. Ramkumar, A. Miglio, M. J. van Setten, D. Waroquiers, G. Hautier and G.-M. Rignanese, *Phys. Rev. Mater.*, 2018, **2**, 085403.

24 S. Hadke, W. Chen, J. M. R. Tan, M. Guc, V. Izquierdo-Roca, G.-M. Rignanese, G. Hautier and L. H. Wong, *J. Mater. Chem. A*, 2019, **7**, 26927–26933.

25 X. Xu and H. Jiang, *J. Chem. Phys.*, 2019, **150**, 034102.

26 J. J. Cordell, J. Pan, A. C. Tamboli, G. J. Tucker and S. Lany, *Phys. Rev. Mater.*, 2021, **5**, 024604.

27 J. W. D. Connolly and A. R. Williams, *Phys. Rev. B: Condens. Matter Mater. Phys.*, 1983, **27**, 5169–5172.

28 J. J. S. Scragg, L. Choubrac, A. Lafond, T. Ericson and C. Platzer-Björkman, *Appl. Phys. Lett.*, 2014, **104**, 041911.

29 C. J. Bosson, M. T. Birch, D. P. Halliday, K. S. Knight, A. S. Gibbs and P. D. Hatton, *J. Mater. Chem. A*, 2017, **5**, 16672–16680.

30 S. K. Wallace, J. M. Frost and A. Walsh, *J. Mater. Chem. A*, 2019, **7**, 312–321.

31 Y.-F. Zheng, J.-H. Yang and X.-G. Gong, *AIP Adv.*, 2019, **9**, 035248.

32 S. De Wolf, J. Holovsky, S.-J. Moon, P. Löper, B. Niesen, M. Ledinsky, F.-J. Haug, J.-H. Yum and C. Ballif, *J. Phys. Chem. Lett.*, 2014, **5**, 1035–1039.

33 S. Chen, A. Walsh, X.-G. Gong and S.-H. Wei, *Adv. Mater.*, 2013, **25**, 1522–1539.

34 D. Han, Y. Y. Sun, J. Bang, Y. Y. Zhang, H.-B. Sun, X.-B. Li and S. B. Zhang, *Phys. Rev. B: Condens. Matter Mater. Phys.*, 2013, **87**, 155206.

35 Y. S. Yee, B. Magyari-Köpe, Y. Nishi, S. F. Bent and B. M. Clemens, *Phys. Rev. B: Condens. Matter Mater. Phys.*, 2015, **92**, 195201.

36 J. Li, Z.-K. Yuan, S. Chen, X.-G. Gong and S.-H. Wei, *Chem. Mater.*, 2019, **31**, 826–833.

37 S. Kim, J.-S. Park, S. Hood and A. Walsh, *J. Mater. Chem. A*, 2019, **7**, 2686–2693.

38 S. Chen, L.-W. Wang, A. Walsh, X. G. Gong and S.-H. Wei, *Appl. Phys. Lett.*, 2012, **101**, 223901.

39 S. Ma, H. Li, J. Hong, H. Wang, X. Lu, Y. Chen, L. Sun, F. Yue, J. W. Tomm, J. Chu and S. Chen, *J. Phys. Chem. Lett.*, 2019, **10**, 7929–7936.

40 D. L. Griscom, *J. Non-Cryst. Solids*, 2006, **352**, 2601–2617.

41 J. L. Gavartin, D. M. Ramo, A. Shluger and G. Bersuker, *ECS Trans.*, 2006, **3**, 277–290.

42 L. D. Whalley, J. M. Frost, B. J. Morgan and A. Walsh, *Phys. Rev. B*, 2019, **99**, 085207.

43 A. Crovetto, S. Kim, M. Fischer, N. Stenger, A. Walsh, I. Chorkendorff and P. C. K. Vesborg, *Energy Environ. Sci.*, 2020, **13**, 3489–3503.

44 P. Zawadzki, A. Zakutayev and S. Lany, *Phys. Rev. Appl.*, 2015, **3**, 034007.

45 U. Rau and J. H. Werner, *Appl. Phys. Lett.*, 2004, **84**, 3735–3737.

46 U. Rau, *Phys. Rev. B: Condens. Matter Mater. Phys.*, 2007, **76**, 085303.

47 U. Rau, U. W. Paetzold and T. Kirchartz, *Phys. Rev. B: Condens. Matter Mater. Phys.*, 2014, **90**, 035211.

48 S. Kim, J. A. Márquez, T. Unold and A. Walsh, *Energy Environ. Sci.*, 2020, **13**, 1481–1491.

49 W. Shockley and W. T. Read, *Phys. Rev.*, 1952, **87**, 835–842.

50 R. N. Hall, *Phys. Rev.*, 1952, **87**, 387.

51 C. J. Hages, A. Redinger, S. Levcenko, H. Hempel, M. J. Koeper, R. Agrawal, D. Greiner, C. A. Kaufmann and T. Unold, *Adv. Energy Mater.*, 2017, **7**, 1700167.

52 C. Yan, J. Huang, K. Sun, S. Johnston, Y. Zhang, H. Sun, A. Pu, M. He, F. Liu, K. Eder, L. Yang, J. M. Cairney, N. J. Ekins-Daukes, Z. Hameiri, J. A. Stride, S. Chen, M. A. Green and X. Hao, *Nat. Energy*, 2018, **3**, 764–772.

53 Y. Ren, N. Ross, J. K. Larsen, K. Rudisch, J. J. S. Scragg and C. Platzer-Björkman, *Chem. Mater.*, 2017, **29**, 3713–3722.

54 E. Chagarov, K. Sardashti, A. C. Kummel, Y. S. Lee, R. Haight and T. S. Gershon, *J. Chem. Phys.*, 2016, **144**, 104704.

55 T. Gershon, K. Sardashti, O. Gunawan, R. Mankad, S. Singh, Y. S. Lee, J. A. Ott, A. Kummel and R. Haight, *Adv. Energy Mater.*, 2016, **6**, 1601182.

56 T. Gershon, Y. S. Lee, P. Antunez, R. Mankad, S. Singh, D. Bishop, O. Gunawan, M. Hopstaken and R. Haight, *Adv. Energy Mater.*, 2016, **6**, 1502468.

57 A. Guchhait, Z. Su, Y. F. Tay, S. Shukla, W. Li, S. W. Leow, J. M. R. Tan, S. Lie, O. Gunawan and L. H. Wong, *ACS Energy Lett.*, 2016, **1**, 1256–1261.

58 Y. Zhao, X. Han, B. Xu, W. Li, J. Li, J. Li, M. Wang, C. Dong, P. Ju and J. Li, *IEEE J. Photovolt.*, 2017, **7**, 874–881.

59 S. H. Hadke, S. Levcenko, S. Lie, C. J. Hages, J. A. Márquez, T. Unold and L. H. Wong, *Adv. Energy Mater.*, 2018, **8**, 1802540.

60 Z.-Y. Xiao, Y.-F. Li, B. Yao, R. Deng, Z.-H. Ding, T. Wu, G. Yang, C.-R. Li, Z.-Y. Dong, L. Liu, L.-G. Zhang and H.-F. Zhao, *J. Appl. Phys.*, 2013, **114**, 183506.

61 Z. Su, J. M. R. Tan, X. Li, X. Zeng, S. K. Batabyal and L. H. Wong, *Adv. Energy Mater.*, 2015, **5**, 1500682.

62 C. Yan, K. Sun, J. Huang, S. Johnston, F. Liu, B. P. Veettil, K. Sun, A. Pu, F. Zhou, J. A. Stride, M. A. Green and X. Hao, *ACS Energy Lett.*, 2017, **2**, 930–936.

63 Z. Su, G. Liang, P. Fan, J. Luo, Z. Zheng, Z. Xie, W. Wang, S. Chen, J. Hu, Y. Wei, C. Yan, J. Huang, X. Hao and F. Liu, *Adv. Mater.*, 2020, **32**, 2000121.

64 S. Kim, K. M. Kim, H. Tampo, H. Shibata, K. Matsubara and S. Niki, *Sol. Energy Mater. Sol.*, 2016, **144**, 488–492.

65 A. D. Collord and H. W. Hillhouse, *Chem. Mater.*, 2016, **28**, 2067–2073.

66 S. Kim, K. M. Kim, H. Tampo, H. Shibata and S. Niki, *Appl. Phys. Express*, 2016, **9**, 102301.

67 L. Choubrac, M. Bär, X. Kozina, R. Félix, R. G. Wilks, G. Brammertz, S. Levcenko, L. Arzel, N. Barreau, S. Harel, M. Meuris and B. Vermang, *ACS Appl. Energy Mater.*, 2020, **3**, 5830–5839.

This journal is © The Royal Society of Chemistry 2021

Energy Environ. Sci., 2021, **14**, 3567–3578 | **3577**

View Article Online

Paper   **Energy & Environmental Science**

68 S. Schorr, G. Gurieva, M. Guc, M. Dimitrievska, A. Pérez-Rodríguez, V. Izquierdo-Roca, C. S. Schnohr, J. Kim, W. Jo and J. M. Merino, *J. Phys. Energy*, 2020, **2**, 012002.

69 *CASM v0.2.1.*, 2017, available from https://github.com/prisms-center/CASMcode.

70 B. Puchala and A. Van der Ven, *Phys. Rev. B: Condens. Matter Mater. Phys.*, 2013, **88**, 094108.

71 J. C. Thomas and A. Van der Ven, *Phys. Rev. B: Condens. Matter Mater. Phys.*, 2013, **88**, 214111.

72 A. Van der Ven, J. Thomas, B. Puchala and A. Natarajan, *Annu. Rev. Mater. Res.*, 2018, **48**, 27–55.

73 G. Kresse and J. Furthmüller, *Comput. Mater. Sci*, 1996, **6**, 15–50.

74 G. Kresse and J. Furthmüller, *Phys. Rev. B: Condens. Matter Mater. Phys.*, 1996, **54**, 11169–11186.

75 P. Giannozzi, S. Baroni, N. Bonini, M. Calandra, R. Car, C. Cavazzoni, D. Ceresoli, G. L. Chiarotti, M. Cococcioni, I. Dabo, A. Dal Corso, S. de Gironcoli, S. Fabris, G. Fratesi, R. Gebauer, U. Gerstmann, C. Gougoussis, A. Kokalj, M. Lazzeri, L. Martin-Samos, N. Marzari, F. Mauri, R. Mazzarello, S. Paolini, A. Pasquarello, L. Paulatto, C. Sbraccia, S. Scandolo, G. Sclauzero, A. P. Seitsonen, A. Smogunov, P. Umari and R. M. Wentzcovitch, *J. Phys.: Condens. Matter*, 2009, **21**, 395502.

76 P. Giannozzi, O. Andreussi, T. Brumme, O. Bunau, M. B. Nardelli, M. Calandra, R. Car, C. Cavazzoni, D. Ceresoli, M. Cococcioni, N. Colonna, I. Carnimeo, A. D. Corso, S. de Gironcoli, P. Delugas, R. A. D. Jr, A. Ferretti, A. Floris, G. Fratesi, G. Fugallo, R. Gebauer, U. Gerstmann, F. Giustino, T. Gorni, J. Jia, M. Kawamura, H.-Y. Ko, A. Kokalj, E. Küçükbenli, M. Lazzeri, M. Marsili, N. Marzari, F. Mauri, N. L. Nguyen, H.-V. Nguyen, A. O. de-la Roza, L. Paulatto, S. Poncé, D. Rocca, R. Sabatini, B. Santra, M. Schlipf, A. P. Seitsonen, A. Smogunov, I. Timrov, T. Thonhauser, P. Umari, N. Vast, X. Wu and S. Baroni, *J. Phys.: Condens. Matter*, 2017, **29**, 465901.

77 L. Lin, *J. Chem. Theory Comput.*, 2016, **12**, 2242–2249.

78 I. Carnimeo, S. Baroni and P. Giannozzi, *Electron. Struct.*, 2019, **1**, 015009.

79 D. R. Hamann, *Phys. Rev. B: Condens. Matter Mater. Phys.*, 2013, **88**, 085117.

80 D. R. Hamann, *Phys. Rev. B*, 2017, **95**, 239906.

81 M. van Setten, M. Giantomassi, E. Bousquet, M. Verstraete, D. Hamann, X. Gonze and G.-M. Rignanese, *Comput. Phys. Commun.*, 2018, **226**, 39–54.

82 C. Freysoldt, J. Neugebauer and C. G. Van de Walle, *Phys. Rev. Lett.*, 2009, **102**, 016402.

83 C. Freysoldt, J. Neugebauer and C. G. Van de Walle, *Phys. Status Solidi B*, 2011, **248**, 1067–1076.

84 H.-P. Komsa, T. T. Rantala and A. Pasquarello, *Phys. Rev. B: Condens. Matter Mater. Phys.*, 2012, **86**, 045112.

85 S. Kim, J.-S. Park and A. Walsh, *ACS Energy Lett.*, 2018, **3**, 496–500.

86 T. Kirchartz and U. Rau, *Adv. Energy Mater.*, 2018, **8**, 1703385.